Single ionization of molecular iodine

Dale L. Smith,[1] Vincent Tagliamonti,[2] James Dragan,[3] and George N. Gibson[1,*]
[1]*Department of Physics, University of Connecticut, Storrs, Connecticut 06269, USA*
[2]*Department of Physics and Astronomy, Stony Brook University, Stony Brook, New York 11794-3800, USA*
[3]*Department of Physics and Astronomy, Northwestern University, Evanston, Illinois 60208, USA*
(Received 24 October 2016; published 24 January 2017)

We performed a study of the single ionization of iodine, I_2 over a range of wavelengths. Single ionization of I_2 is unexpectedly found to have a contribution from inner molecular orbitals involving the 5*s* electrons. The $I + I^+$ dissociation channel was recorded through velocity map imaging, and the kinetic-energy release of each channel was determined with two-dimensional fitting of the images. Most of the measured kinetic-energy data were inconsistent with ionization to the *X*, *A*, and *B* states of I_2^+, implying ionization from deeper orbitals. A pump-probe Fourier transform technique was used to look for modulation at the *X*- and *A*-state vibrational frequencies to see if they were intermediate states in a two-step process. *X*- and *A*-state modulation was seen only for kinetic-energy releases below 0.2 eV, consistent with dissociation through the *B* state. From these results and intensity-, polarization-, and wavelength-dependent experiments we found no evidence of bond softening, electron rescattering, or photon mediation through the *X* or *A* states to higher-energy single-ionization channels.

DOI: 10.1103/PhysRevA.95.013410

I. INTRODUCTION

While the single-electron ionization rates of atoms in strong fields are relatively well understood [1,2], molecules have attracted attention over the years due to their additional degrees of freedom (vibrational, rotational, and electronic). These degrees of freedom allow for the study of the dependence of ionization on angle and internuclear separation [3,4]. Bond softening and enhanced ionization are two such prominent effects that have been predicted and observed [5–9]. More recently, the electronic degrees of freedom have attracted more attention. For example, in molecules, inner-valence orbitals can play an important role, as they lie less deeply bound than the corresponding inner shells in atoms [10–12]. Ionization of an inner orbital will leave the molecular ion in an excited state affecting all subsequent strong-field phenomena, such as rescattering, high-harmonic generation (HHG), and multiple ionization. Moreover, given the highly nonlinear nature of these interactions, the possibility arises that understanding these strong-field effects may, in turn, provide information about the structure of the molecular orbitals (MO), using techniques such as quantum tomography [13] and electron diffraction [14]. Given the likelihood that ionization will not be selective from a particular orbital but, rather, produce a hole involving multiple orbitals, ultrafast dynamics may be introduced and measured [15,16]. Nevertheless, all of these questions and opportunities rely on knowing which orbitals are involved in the interaction.

As mentioned above, inner-orbital ionization will lead to a molecular ion in an excited state. As it turns out, ample evidence has accumulated over the years showing excitation of the molecules through strong-field ionization. Experiments include the observation of charge asymmetric dissociation of even-charged molecular ions [17–19], observation of molecular fluorescence in the vacuum ultraviolet (VUV) spectral region [11], electron spectroscopy directly showing ionization of the highest occupied molecular orbital (HOMO) -2 in N_2 [10], and the dramatic manifestation of excitation through lasing in the atmosphere on a transition from a state possibly produced through ionization of the HOMO-2 orbital [20,21]. While the excitation of molecules could be produced through inner-orbital ionization, it does not prove that this is the mechanism. Another experiment provides a closer link [22]. VUV radiation from atomic fragments following strong-field ionization revealed a clear pattern: radiation from plasma excitation could be identified with Rydberg-type excitations of the atomic ions, while radiation from the direct laser-molecule interaction was uniquely identified with atomic ion states involving one or two holes in the 2*s* shell. This implies a coupling with the molecular orbitals formed from the 2*s*, not just the 2*p*, electrons. This also sets the energy scale of the excitation of at least 10–20 eV, and indeed, VUV fluorescence from strong-field ionization was observed in this energy range [23]. Why these deep inner orbitals couple strongly to the laser field remains to be explored and understood.

While light simple molecules, such as N_2, O_2, CO_2, and SO_2, have been extensively studied [19,24–27], it is important to expand the range of molecules studied to gain a deeper understanding of the strong-field interaction. One extension is to more complex light molecules, such as C_2H_2, C_2H_4, C_6H_6, etc. In these molecules there are numerous low-lying orbitals that can readily interact with the laser field [28,29]. However, in light molecules, the ionization and dissociation generally happen at the same time during the laser pulse because the light nuclei move fast. In this paper, we take a different approach and look at a heavy diatomic molecule: iodine. Like the light polyatomic molecules, I_2 has low-lying accessible molecular orbitals [30,31]. However, its nuclear motion is very slow due to its large mass, and we can cleanly decouple ionization from dissociation. In this case, the kinetic energy of the atomic fragments following ionization should be easily interpreted through energy conservation with the known potential-energy curves at the equilibrium internuclear separation and the atomic dissociation limits. I_2 is interesting as the orbitals are much harder to calculate [30], and insight from strong-field

*george.gibson@uconn.edu

experiments may be useful. In addition, I_2 immediately stands out compared to light diatomic molecules, as it is more likely to dissociate after ionization than remain a molecular ion, unlike light molecules, which tend to remain intact [32].

In this paper, we measure the kinetic-energy release (KER) of the $I^+ + I$ (1,0) dissociation channel [throughout this paper (n,m) designates the $I_2^{(n+m)+} \rightarrow I^{n+} + I^{m+}$ dissociation channel] of I_2^+ over a wide range of wavelengths (800–400 nm) with ultrashort (40 fs) laser pulses. The vibrational period of the I_2^+ ground state is 139 fs [33]. Given the fact that most ionization will occur at the peak of the pulse, very little internuclear motion will occur during ionization. This means that bond softening should not play a role. In this case, the KER will depend only on the energy of the initial state of I_2^+ and the dissociation limits. Ionization of the HOMO populates the $X_{1/2,3/2}$ states, and that of the HOMO-1 populates the $A_{1/2,3/2}$ states [33,34]. All of these states remain bound when populated at the equilibrium internuclear separation R_e of the I_2 ground state, resulting in no dissociation. Ionization of the HOMO-2 populates the B state that will dissociate in the range of 0–0.15 eV, which is easily seen in the data. However, our attention will be focused on the majority of the ionization signal, which produces fragments with KERs above 0.5 eV. These channels cannot be associated with the three least bound orbitals based on the KER data and a pump-probe technique described below. For this reason, we conclude that the bulk of the ionization involves the deeper orbitals built on the $5s$ electrons, reminiscent of the ionization of the $2s$ electrons in N_2, discussed above. The $5s$ electrons in atomic iodine lie about 10 eV below the $5p$ electrons, and so it remains an open question as to why there is such strong coupling to the deeply bound inner orbitals in both the light and heavy homonuclear diatomics.

II. EXPERIMENT

The experimental configuration is shown schematically in Fig 1. To produce photoionization and photodissociation a Spectra Physics Spitfire 800-nm, 40-fs, 800-μJ, 1-kHz Ti:sapphire laser is used [12]. This pumps a dispersion-compensated Light Conversion TOPAS optical parametric amplifier (OPA) to produce 450- to 750-nm photons with a pulse duration of 45 fs. The pulse duration, spectrum, and beam profile out of the OPA is checked for each wavelength. Also, 400-nm photons are generated through second-harmonic generation in a type-I 500-μm-thick barium borate (BBO) crystal. A broadband beam splitter splits the beam path into a pump-probe configuration for certain experiments. The higher transmission from the beam splitter is sent to the BBO or the OPA. A motorized stage is used to introduce temporal delay between the pump and probe. After the OPA and delay stage the pump and probe are recombined collinearly and sent into the vacuum chamber. Pump-probe experiments were run at only 800 nm with a delay of 25 fs per image and a total scan time of 1300 fs. In this configuration an 800-nm beam splitter was used for the recombining mirror. For single pulses from the OPA a silver mirror was used, and for single pulses from the BBO the mirror was removed. In the chamber the beam is focused using a spherical mirror with a focal length of 7.6 cm. The focus intensity ranges from 6×10^{13} to 1×10^{15} W/cm^2 depending on wavelength and energy.

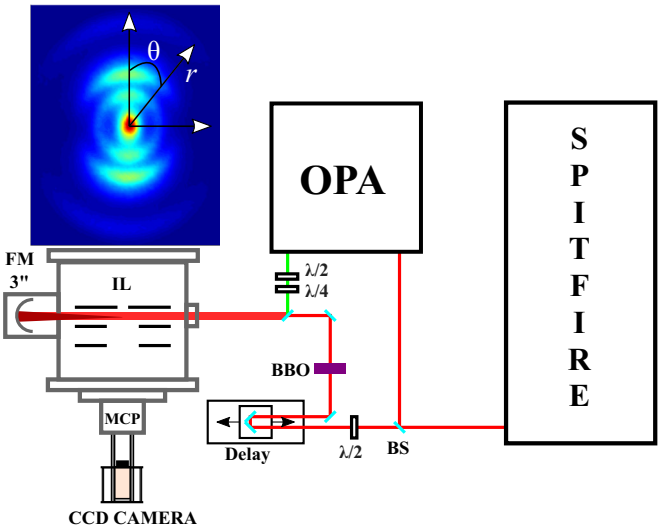

FIG. 1. Experimental setup. BS: beam splitter, $\lambda/2$: half-wave plate, $\lambda/4$: quarter-wave plate, BBO: barium borate crystal, Delay: delay stage, OPA: optical parametric amplifier, IL: ion lens, FM: focusing mirror, MCP: microchannel plates and phosphor screen. The mirror after the OPA is removed when using the BBO crystal. An example VMI image is shown at the top.

Room-temperature iodine is diffused into the chamber through a leak valve. The chamber is pumped by a turbo molecular pump with a typical background pressure of 5×10^{-9} Torr. The I_2 pressure is set between 10^{-8} and 10^{-7} Torr, depending on the experiment. A three-element velocity map imaging (VMI) ion lens configuration similar to the one used by Eppink and Parker [35] is used to accelerate the cations. A microchannel plate (MCP) and phosphor screen are used to detect the cations, which are imaged by a CCD camera at 20 frames/s. The MCP is gated using a pulse generator [36]. In order to record the data in ion-counting mode each image is thresholded to remove noise, and the remaining pixel values are set to 1 to remove MCP fluctuations. A single frame contains 50 laser shots; however, since we maintain a relatively low iodine pressure and low intensities, we rarely see more than two ion counts per 50 laser shots. Anywhere from 100 to 50 000 images are summed depending on the experiment. Since iodine is heavy and therefore slow in time of flight (TOF), we are able to slice the VMI images using dc gating [37,38].

The momentum space image is transformed to energy space using the following known conversion:

$$y_E = A y_p^2, \tag{1}$$

where y_E is the total KER of the ion and its dissociation partner (in eV), y_p is the momentum (in units of pixels in the image), and A is a scale factor. Using five block-averaged images, we find $A = 1/700$ eV/pixel^2 based on the known total KER of the (1,1) channel, 4.7 eV [18,39]. Figure 2 shows a sample of typical VMI images for four wavelengths and identifies the I^+ channels as well as the I_2^{2+} channels.

III. DATA ANALYSIS

To identify the KER of the various channels in the VMI images we employ the following fitting algorithm. First, to improve statistics, we five block averaged and folded the

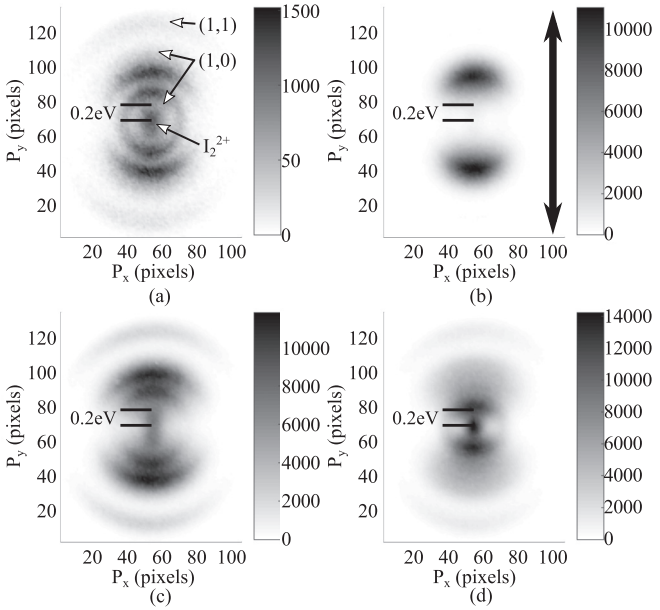

FIG. 2. Typical single-ionization images at various wavelengths: (a) 487 nm, (b) 520 nm, (c) 691 nm, and (d) 800 nm. The arrow in (b) shows the polarization axis used for all images. All images are five block averaged. The I^+ channels and I_2^{2+} are identified in (a). The amplitude of the signal is displayed in arbitrary units.

images in quadrature [40]. We then fit each image using an in-house MATLAB program. For the angular dependence the fit uses the sum of the first four even Legendre polynomials. A Gaussian function of the radius r and the polar angle θ is used for the radial dependence:

$$S(r,\theta) = \sum_{i=1}^{N} \left\{ \exp\left(-\frac{1}{2}\left[\frac{r - r_i}{w} \right]^2 \right) [a_{1,i} L_0(\theta)_i + a_{2,i} L_2(\theta)_i + a_{3,i} L_4(\theta)_i + a_{4,i} L_6(\theta)_i] \right\}. \quad (2)$$

Here i runs from 1 to the number of fit curves needed N, r_i is the radius of the fit curve, w is the width, L_n is the nth Legendre polynomial, and $a_{j,i}$ is the amplitude which scales each of the $j = 1,2,3,4$ Legendre polynomials for i fit curves. A χ^2 test is used to find the best fit. For this experiment we found six fit functions are needed to achieve the best fit. Example fit images are shown in Fig. 3. We required six functions for the following reasons: The I_2^{2+} peak at the center of the image has a fixed thermal width for constant repeller voltage. Since the width is dependent on charge and independent of the cation mass, we experimentally determined the width of I_2^{2+} using Ne^{2+} and Ar^{2+}. We find the width of the thermal peak to be 0.0275 eV [41]. This width agrees with calculations and simulations in SIMION. For each image fit the thermal peak is fixed at zero radius, and its width is fixed to the previously mentioned value. Also, for the thermal peak, the amplitude of the L_0 function is allowed to vary, while the amplitudes for L_2, L_4, and L_6 are set to zero. A second function was used for the (1,1) channel present in all the images. A third function accounted for the low-energy peak with a relatively constant KER, which is described in the next section. The remaining structure in the (1,0) dissociation channel required three functions to fit well, as shown in Fig. 4. It is not at all clear from the one-dimensional (1D) line outs that three functions are needed. However, the three channels differentiated themselves in the two-dimensional (2D) fits and were consistently needed for all wavelengths.

To attempt to understand the dissociation pathways in the (1,0) channels 2D fast Fourier transform (FFT) spectroscopy is performed on pump-probe VMI data. The idea is that the higher-energy KER channels may come from a two-step process through the X or A states of the ion. Thus, the X or A states may dissociate through the absorption of one or more photons. If this were the case, then these dissociation channels would be modulated at the vibrational frequency of the X or A state. To perform the 2D FFT each pixel i in image j is converted into a time series running from 1 to j. A 1D FFT is performed on this series, and the value of the FFT corresponding to the frequency of the state of interest is used for the pixel value i. This is done for all pixels in the original

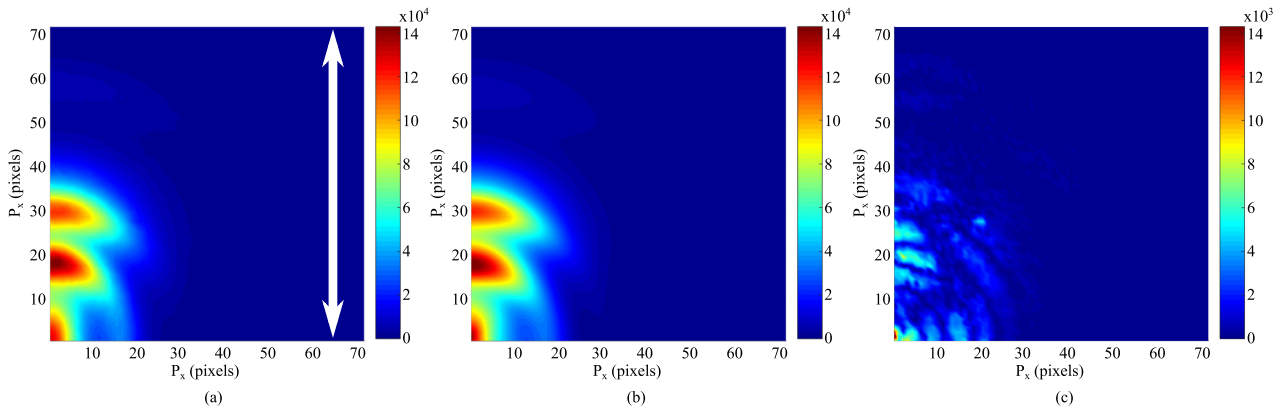

FIG. 3. Typical fit images showing single ionization at 485 nm with vertically polarized light. The z axis is in intensity with arbitrary units. (a) The original image five block averaged and folded in quadrature. The white arrow shows the polarization axis. (b) The fit image. (c) The original image subtracted from the fit image. (a) and (b) have the same intensity scale, while in (c) the scale is magnified by 10 to show the residuals.

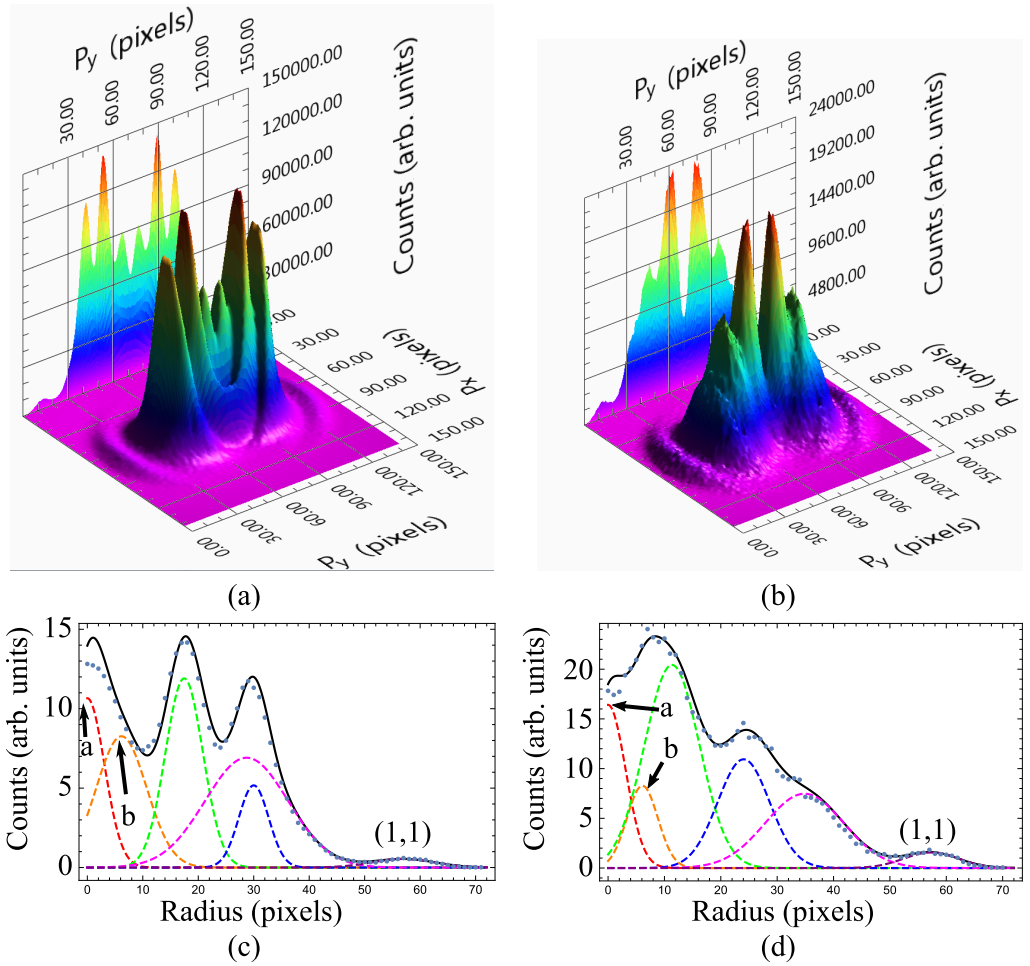

FIG. 4. (a) and (c) A representative 3D image and line out at 485 nm. In this image the B-state peak is clearly visible at low energy. (b) and (d) Representative 3D image and line out at 590 nm. In this image the outer second high-energy peak is just emerging around the bottom of the larger inner high-energy peak. In the 3D image the central I_2^{2+} peak is removed as described in the text, and the line outs are along the $\theta = 0$ direction. In (c) and (d) arrow a labels the thermal I_2^{2+} fit curve and arrow b labels the low KER fit curve, which we will associate with the B state.

image, forming a new 2D FFT image. This allows us to clearly identify X- or A-state modulation in the 2D FFT VMI image. A typical 2D FFT image is shown in Fig. 5.

We considered three sources of error in the KER measurements. First, there is the quality of the fits. We used the standard method of using the curvature of χ^2 in parameter space to estimate the errors in the fit parameters [42]. This gave a relative uncertainty in the KER of 10^{-4}, which sets only a lower bound on the error. Second, we used the repeatability of the KERs for data sets taken at the same wavelength but at different intensities and gas pressures and on different days. This gave an error of 0.125 eV for the (1,1) channel. This agrees nicely with the standard deviation of the measurement of the (1,1) for different wavelengths (again, 0.125 eV), as we do not expect a strong wavelength dependence to the (1,1) KER. Third, there may be a systematic error from the use of Gaussian functions to fit the KER spectrum, as that may not reflect the true KER distribution of a single dissociation channel. However, this error will be independent of the other experimental parameters, such as wavelength, intensity, and pressure. Since the fitting was done in momentum space, we

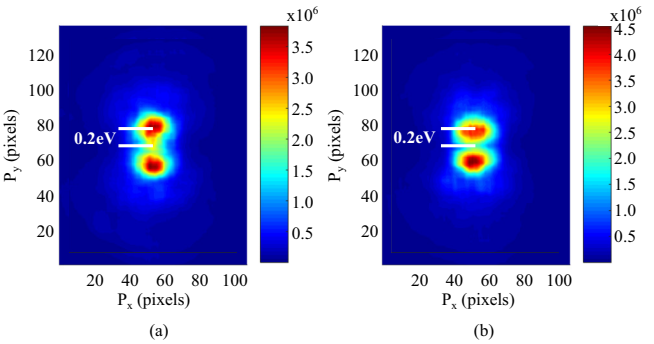

FIG. 5. Example 2D FFT VMI analysis images showing (a) X-state modulation and (b) A-state modulation. The pump and probe are vertically polarized 800-nm light. In addition to five-block averaging these images have also been smoothed to enhance the modulation signal. Also shown is the 0.2 eV radial distance consistent with dissociation through the B state. Note that since a slightly lower repeller voltage was used to magnify the (1,0) channel, these images have been scaled to the same image size as the single-pulse images used in this paper.

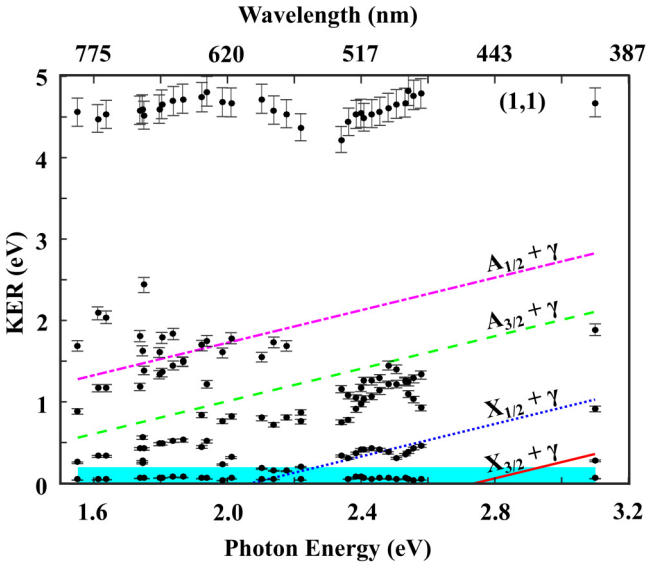

FIG. 6. Plot of fit KER versus 32 photon energies. Fit data are plotted in black. The horizontal blue box shows the B-state dissociation energy range from 0 to 0.15 eV. The slanted lines show the one-photon mediated KER calculated for the X state (3/2 is the solid red line, and 1/2 is the dotted blue line) and the A state (3/2 is the dashed green line, and 1/2 is the dash-dotted purple line) to the $^2P_{3/2} + {}^3P_2$ dissociated $I^+ + I$ state. The data points at 0 eV corresponding to the thermal $I_2{}^{2+}$ are not shown.

scaled the KER uncertainty of 0.125 at 4.7 eV according to $dE = 2\sqrt{2}Apdp$, where E is the energy (in eV), A is the same constant as in Eq. (1), and p is the momentum (in pixels).

IV. RESULTS

In this paper, we are mainly concerned with the KER of the various (1,0) dissociation channels of $I_2{}^+$. In fitting the data, we needed to include the angular distribution and the magnitude of the signal, but we will not consider them further in this paper. Figure 6 shows the main results of the wavelength-dependent study of the dissociation channels. In addition to the dissociation, there is, of course, an $I_2{}^+$ signal not seen in these images. At the top of Fig. 6 is the (1,1) channel. This is relatively constant as a function of wavelength and has been measured by several different groups, producing a KER of 4.7 eV. There is some deviation around photon energies of 2.3 eV, but this is where the OPA crosses over from one mixing scheme to another and will require further study. The rest of the data points in Fig. 6 correspond to individual (1,0) channels.

As mentioned above, to first order, the X and A states of $I_2{}^+$ are bound and will not produce a (1,0) signal. The B state has a binding potential, but if populated at the equilibrium internuclear separation R_e, the wave packet will dissociate, although with very low energy in the range of 0.05–0.15 eV. This can be seen in Fig. 6 at the very bottom of the graph and is produced at every wavelength. So our goal is to understand the rest of the data. Simple ionization of the HOMO, HOMO-1, and HOMO-2 will not give rise to the observed KERs. There are several possible explanations. The first is the simplest and is the one we believe to be correct: ionization occurs

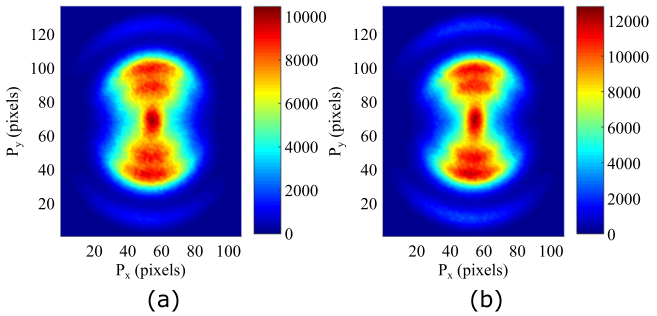

FIG. 7. Example VMI images for the polarization dependence at 661 nm. (a) VMI image with circular polarization. (b) Two VMI images, one with vertical polarization and one with horizontal polarization, summed together.

from deeper orbitals, HOMO-3 and HOMO-4, which involve orbitals built on the 5s electrons. However, before we can make this conclusion, we must consider other possibilities. Rescattering is well known to occur in strong fields and leads to HHG [1], nonsequential double ionization [19,24,43], and hot electrons [44]. It may well lead to excitation. For example, if an electron is ionized from the HOMO, the X state would be populated, but the rescattered electron may excite the molecular ion to a higher state, producing a large KER. However, this can be ruled out by using circular polarization, as shown in Fig. 7. While there are slight differences in the VMI images comparing linear and circular polarizations, the number of channels and corresponding KERs are clearly the same. Thus, the multiplicity of (1,0) channels and their KERs cannot be attributed to rescattering.

The other scenario that does not invoke direct inner-orbital ionization is some postionization interaction with the laser field. This can occur in two limits: first, the cation starts to dissociate while the field is on, or the cation is essentially stationary in the field. In the former case, the cation can encounter laser-induced curve crossings, generally known as bond softening. This is not likely, as iodine is quite heavy and will not move during the laser pulse. Moreover, one would expect an intensity dependence of the KER mediated by bond softening as the magnitude of the laser-induced gap would be intensity dependent. We found no such intensity dependence, and Fig. 8 shows an example of this.

Finally, we must consider one other possibility: if, for example, the A state is populated through ionization of the HOMO-1, the cation may be able to absorb an additional photon and reach a dissociating curve which produces a large KER. However, since the X- and A-state curves are known, one can predict the resulting KER. Furthermore, there should be a linear dependence of the KER on the wavelength. Figure 6 includes these possible KER curves resulting from one-photon absorption from the X or A states. There does seem to be a signal consistent with ionization to the $X_{1/2}$ state plus one photon and perhaps to the $A_{1/2}$ plus one photon. However, this is just a consistency check, and there are several issues: (1) this assumes that there are states available to absorb the photon, which may not be the case, (2) the $A_{3/2} + \gamma$ line is clearly offset from the data, and (3) the $A_{1/2} + \gamma$ line goes roughly through the data points, but a horizontal line at about 1.6 eV would do equally as well.

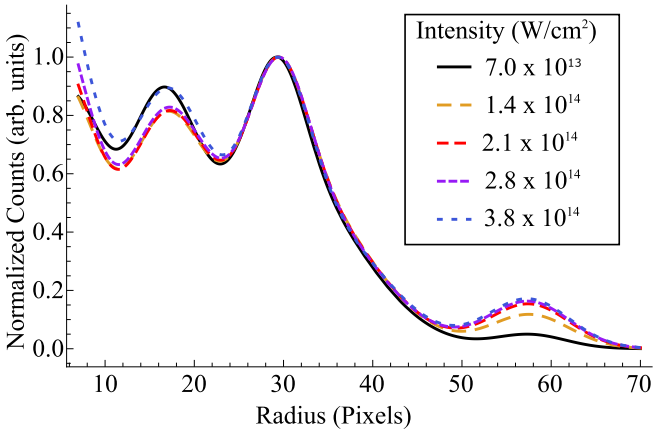

FIG. 8. Fit for one wavelength showing the KER dependence of the peaks for five intensities.

Because it is important to make a definitive conclusion on this possibility, we also performed a more involved experiment. When the X or A states of the cation are populated, they will start to vibrate at their characteristic vibrational frequencies. In order to test whether there is a postionization interaction, we applied a second probe pulse which we scanned in time. Presumably, there will be some R dependence to the postionization interaction, in which case, the signal produced by the absorption of an additional photon will be modulated at the field-free vibration frequency of the intermediate state. To look for this, we performed an FFT of the time series for each pixel in the VMI image. We could then select the frequency of any of the low-lying states of I_2^+ and create an image of the dissociation mediated by that particular state. Indeed, this was the original goal of this series of experiments. We assumed the higher KER channels were the result of such postionization absorption and the FFT VMI images would tell us something about the intermediate state. However, as it turns out, we saw modulation at the X- and A-state frequencies but only in the very low KER region (see Fig. 5). The (1, 0) channels with a KER above 0.2 eV showed no modulation, implying that they came from dissociating potential curves populated directly by the laser field.

V. DISCUSSION

Iodine has 106 electrons in the following MO structure [31]:

$$(\text{core})^{92}\underbrace{(10\sigma_g)^2(10\sigma_u)^2}_{\text{inner valence}}\underbrace{(11\sigma_g)^2(6\pi_u)^4(6\pi_g)^4(11\sigma_u)^0}_{\text{outer valence}}. \quad (3)$$

Ionization from an outer-valence MO places the molecule in a particular state of I_2^+: The HOMO ionizes to the X state, HOMO-1 ionizes to the A state, and HOMO-2 ionizes to the B state [33,34]. Figure 9 shows the potential-energy curves for the low-lying states of I_2 and I_2^+. As can be seen, a vertical transition from the ground state of I_2 at the equilibrium internuclear separation will lead to only an unbound state in the I_2^+ B state. The X and A states of I_2^+ will remain bound. Wave-packet simulations show that population in the X and A states can be promoted to the B state and dissociate. This is consistent with the data in Fig. 5.

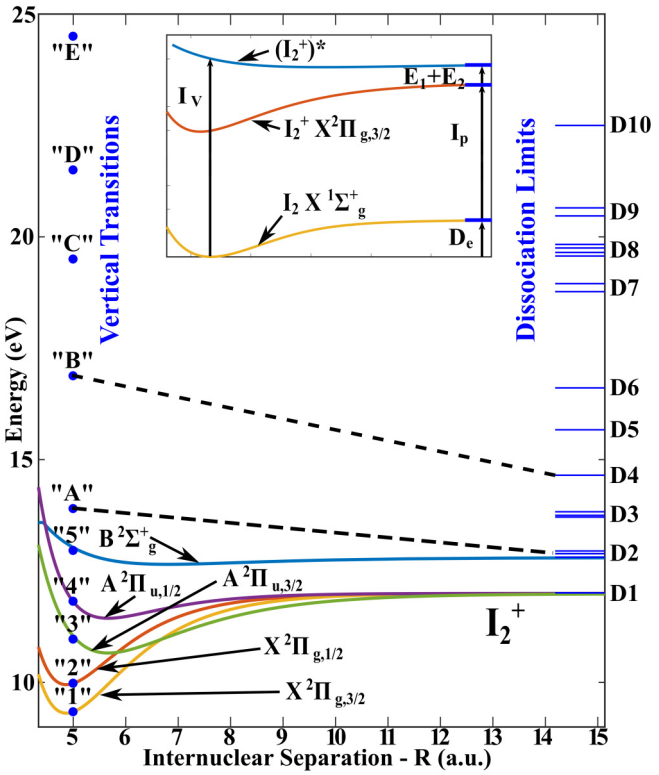

FIG. 9. Potential-energy curves for the X, A, and B states of I_2^+. The I_2 ground state is shown in the inset along with the KER definitions used in Eq. (4). The known Frank-Condon transition energy from the I_2 ground state to I_2^{2+} is shown as blue dots and labeled as in [31]. Plotted on the right-hand side are the possible dissociation energies as described in Sec. IV and labeled as in [30]. The dashed lines show two possible dissociation pathways from Table I.

The number of states to which I_2^+ can dissociate is surprisingly limited due to energy-conservation restrictions. These states are even further limited by the known KER of the (1, 0) channel in which we are interested. This puts a limit on the KER that we expect to see. Through energy conservation we can identify the KER of the direct ionization and dissociation states:

$$E_K = I_V - [E_1 + E_2 + I_p + D_e], \quad (4)$$

where E_K is the KER, I_V is the vertical excitation energy of I_2 to various states of I_2^+, E_1 and E_2 are the internal energies of the two atomic iodine fragments, I_p is the ionization potential of atomic iodine, and D_e is the dissociation energy of the I_2 ground state. See the inset in Fig. 9. I_2 has an ionization potential of 10.45 eV. The dissociation energy of I_2 is 1.57 eV.

Using Eq. (4) and the ionization potentials and dissociation limits of iodine, we can put limits on the KER we expect to see. The ionization potentials of I_2 have been measured using electron-momentum spectroscopy (EMS) and photoelectron spectroscopy (PES) [31,45]. These values are plotted in Fig. 9. The dissociation limits are set by the known atomic energy levels [46]. As an example we look at the B-state KER. The B state dissociates to the D_2 manifold [30]. The D_2 limit has three atomic configurations, giving three possible dissociation

TABLE I. Some possible combinations of the dissociation of I_2 to atomic fragments. DL is the dissociation limit as labeled in [30], and I_p is the atomic ionization potential level as labeled in [31], where level 5 corresponds to the B state of I_2^+. We average the D_2, D_3, and D_7 manifolds. D_2 and D_3 have three possible dissociation limits, while D_7 has two possible dissociation limits. We show only possible KER which falls in the (1,0) range of 0.0 to 3.0 eV. Atomic levels are from Ref. [46].

	DL					
I_p	D_2	D_3	D_4	D_5	D_6	D_7
5	0.06[a]					
A	1.01	0.12				
B			2.21	1.20	0.26	
C					2.74	0.50
						1.35
D						2.67

[a]This value uses the PES data given in [45] since the EMS energies [31] for the B state do not dissociate.

energies. The B-state ionization potential is 12.95 eV as given by PES. This gives the following KER values: 0.14 eV for $^2P_{3/2} + {}^3P_0$, 0.05 eV for $^2P_{3/2} + {}^3P_1$, and 0.00 eV for $^2P_{1/2} + {}^3P_2$. As can be seen in Fig. 6, we find the KER to be within this range [47]. We can also see that there is a flat response versus the photon energy only for the low-energy B-state dissociation and the (1, 1) channel. Allowing for the possibility of photon-assisted dissociation, which adds $n\hbar\omega$, where $n = 1,2,\ldots$, to Eq. (4), we can attempt to identify some of the channels with the X or A state of I_2^+ as discussed above. It can be seen in Fig. 6 that these channels do not fit well with the possible KER of the photon-mediated X or A state except possibly the $X_{1/2}$ state. The pump-probe data, as shown in Fig. 5, confirm this result since they show only X- and A-state modulation in the low-energy B-state dissociation channel. There is no modulation of the high-KER (1,0) channel in the 2D FFT spectrum.

Nuclear wave-function simulations of I_2^+ show that the X and A states do impress modulation onto the B-state dissociation and that the B state dissociates at low energy around 0.2 eV. The simulations do not produce any high-KER dissociation, which is consistent with the investigation results above. Thus, in order to understand the high-energy dissociation channels, we must consider additional initial states (blue dots in Fig. 9) and dissociation limits ($D_3, D_4, \ldots$). Table I summarizes possible KERs from the known initial and final states that fall within the measured range. We are not claiming a precise identification. Rather, we are showing that dissociation pathways exist that fit the data.

VI. CONCLUSION

We have completed an exhaustive study of the dissociation of I_2^+. In this study we have ruled out electron rescattering and bond softening since there was no polarization or intensity dependence. We have found that single ionization in a strong field to high-KER (1,0) channels is not consistent with dissociation through the X, A, or B states. However, low-energy KER does occur through the B state. This implies that single ionization to the high-KER (1,0) channel does not appear to come about through ionization of the HOMO, HOMO-1, or HOMO-2 but is consistent with ionization coming from a deeper HOMO-3 or HOMO-4 formed from the 5s electrons. Further work is needed to identify the exact dissociation pathways and the orbitals involved.

ACKNOWLEDGMENTS

We would like to thank T. Weinacht for beneficial conversations. We would also like to acknowledge our support from the NSF under Grant No. NSF-PHYS-1306845.

[1] P. B. Corkum, Phys. Rev. Lett. **71**, 1994 (1993).
[2] B. Walker, B. Sheehy, L. F. DiMauro, P. Agostini, K. J. Schafer, and K. C. Kulander, Phys. Rev. Lett. **73**, 1227 (1994).
[3] H. Chen, L. Fang, V. Tagliamonti, and G. N. Gibson, Phys. Rev. A **84**, 043427 (2011).
[4] A. Saenz, J. Phys. B **33**, 4365 (2000).
[5] P. H. Bucksbaum, A. Zavriyev, H. G. Muller, and D. W. Schumacher, Phys. Rev. Lett. **64**, 1883 (1990).
[6] A. D. Bandrauk and M. L. Sink, J. Chem. Phys. **74**, 1110 (1981).
[7] T. Zuo and A. D. Bandrauk, Phys. Rev. A **52**, R2511(R) (1995).
[8] T. Seideman, M. Y. Ivanov, and P. B. Corkum, Phys. Rev. Lett. **75**, 2819 (1995).
[9] E. Constant, H. Stapelfeldt, and P. B. Corkum, Phys. Rev. Lett. **76**, 4140 (1996).
[10] G. N. Gibson, R. R. Freeman, and T. J. McIlrath, Phys. Rev. Lett. **67**, 1230 (1991).
[11] G. Gibson, T. S. Luk, A. McPherson, K. Boyer, and C. K. Rhodes, Phys. Rev. A **40**, 2378 (1989).
[12] L. Fang and G. N. Gibson, Phys. Rev. A **75**, 063410 (2007).
[13] J. Itatani, J. Levesque, D. Zeidler, H. Niikura, H. Pépin, J. C. Kieffer, P. B. Corkum, and D. M. Villeneuve, Nature (London) **432**, 867 (2004).
[14] T. Zuo, A. Bandrauk, and P. Corkum, Chem. Phys. Lett. **259**, 313 (1996).
[15] T. Ergler, B. Feuerstein, A. Rudenko, K. Zrost, C. D. Schröter, R. Moshammer, and J. Ullrich, Phys. Rev. Lett. **97**, 103004 (2006).
[16] E. Goll, G. Wunner, and A. Saenz, Phys. Rev. Lett. **97**, 103003 (2006).
[17] D. T. Strickland, Y. Beaudoin, P. Dietrich, and P. B. Corkum, Phys. Rev. Lett. **68**, 2755 (1992).
[18] G. N. Gibson, M. Li, C. Guo, and J. P. Nibarger, Phys. Rev. A **58**, 4723 (1998).
[19] C. Guo, M. Li, and G. N. Gibson, Phys. Rev. Lett. **82**, 2492 (1999).
[20] Q. Luo, W. Liu, and S. Chin, Appl. Phys. B **76**, 337 (2003).
[21] D. Kartashov, S. Ališauskas, G. Andriukaitis, A. Pugžlys, M. Shneider, A. Zheltikov, S. L. Chin, and A. Baltuška, Phys. Rev. A **86**, 033831 (2012).
[22] R. N. Coffee and G. N. Gibson, Phys. Rev. A **69**, 053407 (2004).
[23] R. N. Coffee and G. N. Gibson, Phys. Rev. A **72**, 011401 (2005).
[24] C. Guo, M. Li, J. P. Nibarger, and G. N. Gibson, Phys. Rev. A **61**, 033413 (2000).
[25] E. G. Champenois, N. H. Shivaram, T. W. Wright, C.-S. Yang, A. Belkacem, and J. P. Cryan, J. Chem. Phys. **144**, 014303 (2016).

[26] C. Cornaggia, M. Schmidt, and D. Normand, J. Phys. B **27**, L123 (1994).
[27] C. Cornaggia, F. Salin, and C. L. Blanc, J. Phys. B **29**, L749 (1996).
[28] D. E. Eastman and J. E. Demuth, Jpn. J. Appl. Phys. **13**, 827 (1974).
[29] F. Feixas, J. Vandenbussche, P. Bultinck, E. Matito, and M. Sola, Phys. Chem. Chem. Phys. **13**, 20690 (2011).
[30] W. A. de Jong, L. Visscher, and W. C. Nieuwpoort, J. Chem. Phys. **107**, 9046 (1997).
[31] J. S. Zhu, J. K. Deng, and C. G. Ning, Phys. Rev. A **85**, 052714 (2012).
[32] H. Chen, V. Tagliamonti, and G. N. Gibson, Phys. Rev. Lett. **109**, 193002 (2012).
[33] M. C. R. Cockett, R. J. Donovan, and K. P. Lawley, J. Chem. Phys. **105**, 3347 (1996).
[34] D. C. Frost and C. A. McDowell, Can. J. Chem. **38**, 407 (1960).
[35] A. T. J. B. Eppink and D. H. Parker, Rev. Sci. Instrum. **68**, 3477 (1997).
[36] The phosphor screen is a Beam Imaging Solutions model BOS-40, the CCD camera is a PixeLink model PL-B953U, and the pulse generator is a DEI model PVX-4140.
[37] C. R. Gebhardt, T. P. Rakitzis, P. C. Samartzis, V. Ladopoulos, and T. N. Kitsopoulos, Rev. Sci. Instrum. **72**, 3848 (2001).
[38] D. Townsend, M. P. Minitti, and A. G. Suits, Rev. Sci. Instrum. **74**, 2530 (2003).
[39] J. H. Posthumus, A. J. Giles, M. R. Thompson, W. Shaikh, A. J. Langley, L. J. Frasinski, and K. Codling, J. Phys. B **29**, L525 (1996).
[40] A polar onion peeling program [G. M. Roberts, J. L. Nixon, J. Lecointre, E. Wrede, and J. R. R. Verlet, Rev. Sci. Instrum. **80**, 053104 (2009)] is used to do the folding; however, it is not used to deconvolute the images since the images are sliced.
[41] The energy scale we have used is based on the (1,1) KER. Since this is the total energy of two particles, we must double the thermal width to match the single-particle I_2^{2+} width in the fit.
[42] P. Bevington and D. K. Robinson, *Data Reduction and Error Analysis for the Physical Sciences* (McGraw-Hill, Boston, 2003), pp. 146–150.
[43] C. Guo, M. Li, J. P. Nibarger, and G. N. Gibson, Phys. Rev. A **58**, R4271(R) (1998).
[44] M. B. Smirnov and V. P. Krainov, J. Phys. B **31**, L519 (1998).
[45] A. J. Yencha, M. C. R. Cockett, J. G. Goode, R. J. Donovan, A. Hopkirk, and G. C. King, Chem. Phys. Lett. **229**, 347 (1994).
[46] A. Kramida, Yu. Ralchenko, J. Reader, and NIST ASD Team, NIST Atomic Spectra Database, version 5.3, http://physics.nist.gov/asd.
[47] EMS and PES show slightly different values for the B-state ionization potential [31]. However, the EMS values would not allow for the B state to dissociate. The PES data cover only the first five ionization levels. We have therefore used the EMS values to expand the range of ionization potentials of I_2.